TU Delft

Delft University of Technology

Document Version
Final published version

Licence
Dutch Copyright Act (Article 25fa)

Citation (APA)
Li, Z., Du, W., Yan, X., Gu, C., Wang, X., Tian, T., van Driel, W., Zhang, G., & Fan, J. (2026). Thermal-kinetics-guided sintering-profile optimization and interpretable fracture-mechanism learning for pressureless sintered Ag pastes. *Applied Materials Today*, *50*, Article 103197. https://doi.org/10.1016/j.apmt.2026.103197

Important note
To cite this publication, please use the final published version (if applicable).
Please check the document version above.

Copyright
In case the licence states “Dutch Copyright Act (Article 25fa)”, this publication was made available Green Open Access via the TU Delft Institutional Repository pursuant to Dutch Copyright Act (Article 25fa, the Taverne amendment). This provision does not affect copyright ownership.
Unless copyright is transferred by contract or statute, it remains with the copyright holder.

Sharing and reuse
Other than for strictly personal use, it is not permitted to download, forward or distribute the text or part of it, without the consent of the author(s) and/or copyright holder(s), unless the work is under an open content license such as Creative Commons.

Takedown policy
Please contact us and provide details if you believe this document breaches copyrights.
We will remove access to the work immediately and investigate your claim.

This work is downloaded from Delft University of Technology.

Applied Materials Today 50 (2026) 103197

Contents lists available at ScienceDirect

Applied Materials Today

journal homepage: www.elsevier.com/locate/apmt

Thermal-kinetics-guided sintering-profile optimization and interpretable fracture-mechanism learning for pressureless sintered Ag pastes

Zezhan Li [a], Wei Du [a], Xuyang Yan [a], Chao Gu [a], Xueliang Wang [a], Tiancheng Tian [a], Willem van Driel [b], Guoqi Zhang [b], Jiajie Fan [a,b,c,*]

[a] Shanghai Engineering Technology Research Center of SiC Power Device, College of Intelligent Robotics and Advanced Manufacturing, Fudan University, Shanghai 200433, China
[b] EEMCS Faculty, Delft University of Technology, Delft 2628CD, the Netherlands
[c] Research Institute of Fudan University in Ningbo, Ningbo 315327, China

ARTICLE INFO

Keywords:
Pressureless sintered Ag paste
Thermal kinetics
Fracture-mode distribution
Interpretable machine learning
Multiple-instance learning

ABSTRACT

Pressureless sintered Ag pastes are promising die-attach materials for power electronics, yet practical sintering-profile optimization still relies heavily on trial-and-error, and the link from thermal kinetics to fracture-relevant microstructure and strength remains insufficiently established. In this work, a thermal-kinetics-guided workflow was developed to design paste-specific pressureless sintering profiles for two commercial Ag pastes (a spherical-particle paste and a flake-based paste) and to interpret the resulting strength–fracture response using SEM-based, heterogeneity-aware learning. Multi-heating-rate TGA was used to define the conversion fraction (α), while DSC was used to identify the dominant thermal-event window and extract the characteristic peak temperature for Arrhenius pairing. The TGA-defined conversion evolution was then modeled using a JMAK/Avrami form with Arrhenius temperature dependence to predict the isothermal holding time required to reach a target conversion at a selected dwell temperature. Relative to supplier-recommended profiles, the optimized profiles increased die-shear strength by 35% for the spherical-particle paste and by 206% for the flake-based paste, and promoted a fracture-mode transition from interfacial debonding toward mixed/cohesive fracture. Pearson/Ridge baselines and attention-based multiple-instance learning (MIL) linked strength and fracture-mode distribution to porosity/connectivity-related descriptors; paste-wise normalization mitigated paste-specific baselines and enabled MIL to reveal profile-induced microstructure–performance co-variation. Overall, this study establishes a practical workflow that couples thermal-kinetics-guided profile design with mechanical and fractographic validation and interpretable microstructure–property attribution, supporting mechanism-informed optimization of pressureless sintered Ag die-attach pastes.

1. Introduction

Sintering-based die attach forms a metallic bondline through solid-state diffusion and neck growth among metal particles, offering a high-temperature-capable alternative to conventional joining routes in power-electronic packaging [1,2]. Among candidate materials, silver (Ag) is particularly attractive because it combines excellent thermal/-electrical conductivity with chemical stability, enabling low thermal resistance and robust operation for advanced Si/SiC power modules under increasingly demanding power-density and junction-temperature requirements [1,3,4]. In particular, pressureless sintered Ag pastes eliminate the need for externally applied pressure during bonding, which simplifies tooling/integration and reduces the risk of mechanically damaging fragile dies while retaining the intrinsic high-temperature advantages of Ag-based interconnects [1,3–5].

In practical manufacturing, however, the selection of a temperature-time profile for pressureless Ag pastes is still frequently tuned empirically and adjusted case-by-case [4,5]. Paste chemistry, particle morphology, and the organic system can substantially shift the time-temperature windows for volatilization/decomposition and subsequent neck formation/densification, making profile transferability across paste systems non-trivial [6,7]. As a result, “one-profile-fits-all”

* Corresponding author at: Shanghai Engineering Technology Research Center of SiC Power Device, College of Intelligent Robotics and Advanced Manufacturing, Fudan University, Shanghai 200433, China.
E-mail address: jiajie_fan@fudan.edu.cn (J. Fan).

https://doi.org/10.1016/j.apmt.2026.103197
Received 25 January 2026; Received in revised form 9 March 2026; Accepted 18 March 2026
Available online 28 March 2026
2352-9407/© 2026 Elsevier Ltd. All rights are reserved, including those for text and data mining, AI training, and similar technologies.

schedules can lead to incomplete removal of organics, insufficient neck connectivity, or excessive residual porosity [5,6]. A major obstacle is that the process-structure-property relationship in pressureless sintered Ag is intrinsically heterogeneous. Even under nominally identical processing, local microstructures can vary spatially across a bondline, generating weak regions that dominate crack initiation and propagation [8,9]. Conventional characterization often reports global porosity or a limited number of representative SEM images, which can miss the spatial distribution of defects and local morphological variability that controls damage localization [10]. Therefore, an effective optimization strategy should (i) be guided by transferable thermal/kinetic evidence, (ii) quantify microstructural heterogeneity with physically meaningful descriptors, and (iii) connect local microstructure to both macroscopic strength and fracture-mode tendency in an interpretable manner.

Prior studies have shown that time-dependent deformation and damage accumulation can substantially affect the scatter and reliability of sintered Ag joints under service-like thermo-mechanical histories [11–17]. Reliability tests under harsh thermal cycling and power cycling conditions further report pronounced variations in joint shear strength and accompanying shifts in dominant failure mode, underscoring the reliability sensitivity of pressureless Ag sinter-joining [18]. In parallel, thermal exposure can drive microstructural evolution in the nanoporous Ag network (pore/ligament coarsening, neck growth, and atmosphere-sensitive coarsening mechanisms), accompanied by changes in the dominant failure locus and fracture-mode tendency from interface-dominated debonding toward more cohesive or mixed failure [10,16]. Because these reliability-relevant responses are governed by the coupled evolution of pore/neck connectivity and localized weak regions, an optimized sintering profile is valuable not only for improving peak shear strength but also for stabilizing the microstructure and promoting more robust, reproducible fracture behavior [8–10].

Model-informed optimization of the temperature–time curve provides a practical route to move beyond trial-and-error profile tuning. Prior studies have used thermal analysis (e.g., TGA/DSC) to identify volatilization/burnout windows and to rationalize temperature-controlling profiles for nanosilver pastes used in die-attach interconnections, demonstrating the feasibility of deriving process guidance from measurable thermal signals [19]. When thermal signals are collected at multiple heating rates, recommended kinetic-computation practices (e.g., ICTAC guidance) enable more reproducible extraction of a conversion fraction and model fitting [20]. Using a JMAK/Avrami-type conversion form with Arrhenius temperature dependence, the fitted kinetics can further be translated into a "time--to-target-conversion" map for selecting dwell windows and supporting profile transfer across furnaces [21]. Nevertheless, kinetics-derived conversion targets alone do not guarantee comparable mechanical outcomes, because specimen-level strength and fracture behavior can be dominated by spatially heterogeneous weak spots and by pore/neck-network connectivity [9,10]. This motivates a complementary, heterogeneity-aware route to link local microstructure to specimen-level responses.

To address microstructural heterogeneity explicitly, data-driven analysis of SEM microstructures has gained interest. However, typical supervised models treat each specimen as a single feature vector, implicitly assuming homogeneous structure, which is unsuitable for patch-wise heterogeneous SEM fields where different regions contribute unequally to failure. Multiple-instance learning (MIL) offers a natural formulation: each specimen can be represented as a "bag" of many SEM patches ("instances"), and the model learns to map the bag to a specimen-level target while internally allocating attention to the most influential patches [22]. Moreover, attention-based learning can be equipped with attribution tools such as SHAP or Integrated Gradients to provide interpretable links between microstructural descriptors and predictions [23,24]. Model-agnostic explanation strategies have also been used to complement such interpretations when needed [25]. These tools are valuable for materials processing because they can indicate whether performance changes arise from global microstructural improvement or from mitigation of a small number of critical defects. Although kinetics-guided profile design and microstructure-based learning have been separately explored, an evidence-closed framework that couples thermal-kinetics-driven profile optimization with quantitative strength/fracture validation and heterogeneity-aware, interpretable structure-property attribution remains lacking for pressureless sintered Ag pastes.

To address the above challenges, this work develops an integrated workflow for two commercial pressureless sintered Ag pastes, in which multi-rate thermal analysis is leveraged to extract paste-specific kinetics and translate them into practical temperature–time profile guidance. The effectiveness of the designed profiles is then assessed using complementary evidence from joint strength and fracture-mode tendency. Finally, an interpretable patch-based learning formulation is employed to link spatially heterogeneous microstructural features to specimen-level responses, thereby providing a mechanistic, data-grounded basis for profile optimization and reliability-oriented process design.

2. Materials and methods

2.1. Specimen preparation and characterization

Two commercial pressureless sintered Ag pastes were investigated: Paste A (EXBOND 6810SC-MV, Shanghai Bonotec Electronic Materials Co., Ltd., Shanghai, China) and Paste B (CT2700R7S, KYOCERA Corporation, Tokyo, Japan). For each paste, two sintering schedules were applied: a supplier-recommended profile ("Original") and a kinetics-informed profile ("Optimized"), yielding four conditions (A-Original, A-Optimized, B-Original, and B-Optimized).

Chip-attach specimens were prepared in a sandwich configuration by bonding a SiC MOSFET die (4.13 mm×3.74 mm×0.2 mm) to an Ag-plated Cu substrate/leadframe using the corresponding paste. The nominal bonded area (paste contact area) was 15.45 mm^2 and was used to normalize the die-shear strength. Prior to paste deposition, the die and substrate surfaces were cleaned following standard die-attach practice.

Paste deposition and die placement were performed on an automated die bonder equipped with dispensing capability (Datacon 2200 evo, BESI, The Netherlands). A trial-dispense calibration was conducted before batch fabrication to control the Ag-layer (bondline) thickness to ~43 μm, after which specimens were fabricated in batches using the same dispensing recipe and placement alignment.

To support kinetic computations on thermal-analysis data, thermoanalytical measurements were conducted at multiple heating rates following the general practice recommended by the ICTAC Kinetics Committee [20]. Thermogravimetric analysis (TGA) was performed using a TA Instruments Q50 under N2 atmosphere. Approximately 30–31 mg of as-received paste was placed in an open crucible and spread into a thin layer to reduce internal thermal lag. After equilibration at 30 °C, samples were heated to 500 °C at 5, 10, and 15°C·min^{-1}. A standard dual-purge configuration was used (balance gas 40 mL·min^{-1}; sample gas 60 mL·min^{-1}). Each heating-rate condition was repeated three times and averaged.

Differential scanning calorimetry (DSC) was conducted using a TA Instruments DSC Q2000 under N2 purge (50 mL·min^{-1}). Approximately 30–31 mg of paste was loaded in a standard DSC pan; the paste was spread to ensure stable thermal contact. After equilibration at 30 °C with an isothermal hold of 5 min, samples were heated to 300 °C at 5, 10, and 15 °C·min^{-1}. Each heating-rate condition was repeated three times and averaged.

Pressureless sintering was conducted in a programmable BINDER convection oven (BINDER, FD-115, Germany) under ambient air. For each paste, specimens were processed according to either the Original or Optimized segmented temperature–time schedule (Fig. 4). In total, four furnace runs were executed (A/B × Original/Optimized). To ensure

process reliability, a fine-gauge K-type thermocouple placed near the chip edge was used to log the in-situ temperature trace, confirming that the realized peak temperature agreed with the programmed value within ±3 °C. The Ag-layer thickness was controlled at ~43 μm via dispensing calibration.

SEM images of the sintered Ag layer were acquired using a Hitachi FlexSEM1000 in BSE composition mode at an accelerating voltage of 15 kV (typical working distance ~5.5 mm). Images were collected at a fixed magnification (2000×) with a resolution of 1280× 960 pixels. Specimens were sputter-coated (Au) prior to imaging. The pixel calibration was approximately 0.0468 μm/px. For each specimen, 10 SEM fields of view were acquired using a consistent sampling rule.

2.2. Mechanical testing and fracture characterization

Die shear tests were performed on a bond tester (Dage 4000, Nordson DAGE, UK) equipped with a flat shear tool. The tool was aligned to push against the chip sidewall and loaded at a constant displacement rate of 50 μm·s^{-1} until failure. The shear height was set close to the substrate surface (≈50 μm), and a thin-blade tool (edge width ~100 μm) was used. Related die-attach strength testing for sintered Ag joints has been widely reported [26].

The peak shear force Fmax was recorded, and shear strength was computed by normalizing F_{max} with the nominal bonded area:

$$\tau = \frac{F_{\max}}{A_{chip}} \tag{1}$$

where $A_{chip} = 15.45\ mm^2$. For each condition, $n = 7$ specimens were tested; results are reported as mean ± standard deviation.

After shear testing, fracture surfaces were documented using a digital optical microscope at the macroscale, and representative areas were further examined by SEM at higher magnification. Based on the dominant separation locus and macro fracture appearance, fractures were categorized into three modes: Type A (chip-side interfacial separation), Type B (substrate-side interfacial separation), and Type C (mixed-mode fracture involving substantial cohesive/near-cohesive failure within the sintered Ag layer).

For quantification, each macro fracture image was partitioned into multiple equal-area subregions using a regular grid, and each subregion was assigned a fracture type (A/B/C). Here, the fracture mixedness m (defined in this work) was quantified as the fraction of subregions classified as Type C [8,27]:

$$m = \frac{N_{TypeC}}{N_{total}} \tag{2}$$

where N_{TypeC} is the number of subregions labeled Type C and N_{total} is the total number of labeled subregions. Thus, m ranges from 0 (purely interfacial) to 1 (Type C-dominant).

2.3. Kinetic modeling and profile-design principle

Thermo-analytical measurements were used to construct a conversion-based kinetic workflow, followed by Avrami-type fitting and Arrhenius analysis to enable "time-to-target-conversion" prediction and profile translation, as commonly adopted in thermal-kinetics computations [20,21].

(1) Conversion extraction. For TGA, α was computed by normalizing the mass-loss progress:

$$\alpha(T) = \frac{m_0 - m(t)}{m_0 - m_f} \tag{3}$$

where $m(t)$ is the sample mass at time t, and m_0 and m_f are the initial and final masses over the dominant mass-loss interval. The onset/terminal points (T_o, T_f) were selected consistently from TG/DTG. Time and temperature were mapped by the programmed heating rate. Here, α is used as a thermo-analytical conversion metric for engineering-oriented profile design. The dominant pre-sintering thermal conversion of these pastes is accompanied by measurable mass loss arising from solvent volatilization and organic removal, making the normalized mass-loss fraction a practical and experimentally accessible proxy for the progression of the conversion stage relevant to profile design.

For DSC, baseline-corrected heat-flow curves were analyzed over a consistently defined dominant thermal-event window. For each heating rate, the main peak temperature Tp was extracted as the extremum within this window and was used as the characteristic temperature for Arrhenius pairing.

(2) Avrami (JMAK) fitting. The conversion evolution was modeled using an Avrami-type form: [21].

$$\alpha(T) = 1 - \exp(-kt^n) \tag{4}$$

where k is the apparent rate constant and n is the Avrami exponent. To reduce bias from early-stage surface effects and late-stage diffusion limitation, only the mid-conversion window $\alpha \in [0.1, 0.9]$ was used for regression. For each heating rate, k and n were obtained by least-squares fitting.

(3) Arrhenius analysis. The temperature dependence of k was assumed to follow:

$$k(T) = A\exp\left(-\frac{E}{RT}\right) \tag{5}$$

and the linearized form $\ln k = \ln A - \frac{E}{RT}$ was fitted using the (k, T_p) pairs obtained at different heating rates for each paste. The slope and intercept yielded E and A.

(4) Isothermal holding-time prediction and profile translation. For a selected isothermal dwell temperature T, $k(T)$ was updated using Eq. (5), and the dwell time to reach a target conversion α was obtained by inverting Eq. (4):

$$t = \left[\frac{-\ln(1-\alpha)}{k(T)}\right]^{1/n} \tag{6}$$

Two representative targets ($\alpha = 0.97$ and 0.99) were evaluated to generate a holding-time map versus temperature (Fig. 4a). Here, α = 0.97 and 0.99 were used to define the graphical design space, whereas the α = 0.99 conditions were selected as the final experimental anchors for workflow demonstration under near-complete conversion conditions. To translate the kinetic outcomes into executable furnace programs, a pragmatic rule was adopted: the low-temperature solvent/organic-removal segment followed the original/supplier practice, while the mid-/high-temperature densification-related dwell temperature and duration were adjusted according to the predicted holding-time requirement at the chosen α. Among the candidate α = 0.99 conditions, practical intermediate-temperature anchors were selected, positioned slightly above the dominant DSC peak temperature (approximately 10–20 °C), so as to avoid excessively long dwell times at the lowest-temperature options while remaining below the highest-temperature options. This strategy minimizes new defect sources in the volatile-removal stage while strengthening the densification window. Within the present workflow, the adopted fitting window and simplified kinetic form are considered sufficient for practical profile design, although they should not be overinterpreted as a unique mechanistic description.

2.4. Patch-based microstructure quantification and interpretable analysis

To facilitate reproducibility and readability of the multi-step pipeline, Fig. 1 presents an overview of the SEM patch sampling, descriptor computation, PCA screening/normalization, and subsequent baseline and MIL analyses used in this work.

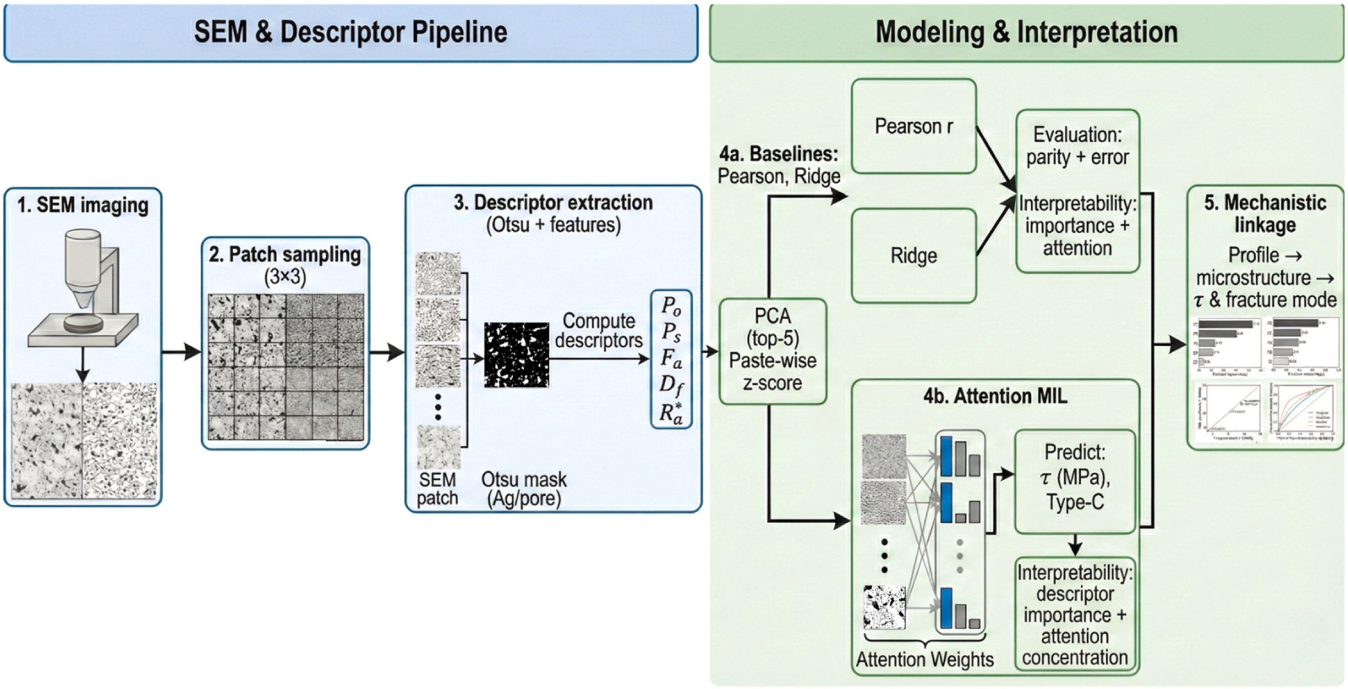


Fig. 1. Overview of the proposed workflow for patch-based SEM descriptor analysis and die-shear strength prediction. SEM images are partitioned into non-overlapping patches and converted into binary masks by Otsu thresholding for descriptor computation (*Po, Ps, Fa, Df,* and R_a^*). The selected descriptors (PCA-screened and paste-wise normalized) are analyzed using Pearson/Ridge baselines and an attention-based multiple-instance learning (MIL) model to link local microstructural heterogeneity to condition-level targets (die-shear strength τ and Type-C fracture fraction), with interpretability provided by descriptor importance and attention concentration.

2.4.1. Patch sampling and microstructural descriptor extraction

A patch-based strategy was used to represent local heterogeneity. Each SEM image was partitioned into 9 non-overlapping patches using a 3× 3 grid (each patch ≈426×320 pixels; physical field ≈19.9 μm × 15.0 μm). Images/patches were grouped into two orthogonal orientation subsets based on acquisition direction: H (horizontal) and V (vertical). Statistics were reported for All patches as well as H- and V-subsets. Microstructure–property correlation and quantitative characterization of sintered Ag microstructures have been discussed in prior works [8,9].

Image processing and descriptor extraction were performed using custom Python scripts (OpenCV + scikit-image). Grayscale images were denoised using Gaussian filtering ($\sigma \approx 1.0$) followed by Otsu thresholding to segment solid vs. pore phases; an automatic inversion rule was applied when needed to ensure consistent identification of the Ag phase. Small segmented objects (area < 30 pixels) were removed to reduce noise sensitivity. From each patch, five core descriptors were computed (Table 1):

(i) P_o (pore fraction, %): area fraction of pores in the binary mask;
(ii) P_s (mean particle size, μm): mean equivalent diameter of connected particle domains;
(iii) F_a (shape factor): compactness/roundness descriptor of connected particle domains computed as $4\pi A/P^2$ and averaged over domains;

(iv) D_f (feature density, μm^{-2}): number density of detected surface/morphological features per unit area, extracted using Laplacian-of-Gaussian blob detection (σ range 1.5–8 pixels; num_sigma = 10; threshold = 0.04).

(v) R_a^* (roughness proxy): gray-level fluctuation–based proxy computed from the mean absolute deviation of detrended grayscale intensity within each patch.

An initial pool of candidate descriptors was extracted and screened by PCA to reduce redundancy. The PCA importance of descriptor j was computed as:

$$I_j = \sum_{k=1}^{N_{PC}} \left(\left| L_{k,j} \right| \cdot EVR_k \right) \tag{7}$$

where $L_{k,j}$ is the loading of descriptor j on principal component k, and EVR_k is the explained-variance ratio of PC k. The five highest-importance descriptors were retained as the core set for downstream analyses (Table 1).

Table 1
SEM-derived microstructural features and symbols.

Feature group	Feature variable	Symbol	Definition
Microstructural features	Pore fraction	P_o	Area fraction of pores
	Mean particle size	P_s	Equivalent diameter of connected particle domains
	Shape factor	F_a	Describing particle roundness and fusion uniformity
	Feature density / area	D_f	Number of features per unit area
	Roughness index	R_a^*	Gray-level fluctuation–based roughness proxy

2.4.2. Pearson/ridge baselines and interpretable multiple instance learning (MIL)

As linear baselines, Pearson correlations were computed between each descriptor and (i) mean shear strength τ and (ii) fracture mixedness m. Ridge regression with standardized inputs was further used to compare effect directions and relative magnitudes under descriptor collinearity [28].

For heterogeneity-aware learning, attention-based multiple instance learning (MIL) models were trained at the bag level [22]. Each condition (bag) was represented by the set of patch descriptors (instances) aggregated from all SEM images under that condition (with All/H/V

subsets analyzed as needed). Two MIL tasks were considered: predicting bag-level τ and predicting bag-level m. Input features were standardized; paste-wise z-score normalization (A-family and B-family separately) was applied to reduce scale bias across paste systems. The MIL model used a lightweight instance embedding (hidden dimension 16) and attention pooling, trained with Adam (learning rate 1×10^{-3}, weight decay 1×10^{-3}) for 1200 epochs with a fixed random seed.

Model interpretability was assessed via (i) gradient-based relative importance of the five descriptors and (ii) attention concentration quantified by cumulative attention-mass curves and top-ranked attention mass. Widely used attribution/interpretability tools were referenced for methodological context [23–25]. Because the current bag-level dataset includes four conditions, MIL outcomes were used primarily as a condition-level, explainable linkage between local microstructural units and specimen-level targets.

3. Results and discussion

3.1. Kinetics-informed profile design

Fig. 2 compares the intrinsic powder morphologies of the two commercial pressureless Ag pastes [29]. Paste A is dominated by near-spherical/quasi-spherical particles with relatively smooth contours (Fig. 2a), while Paste B exhibits finer and more irregular, locally flake-like/angular features (Fig. 2c). The corresponding particle diameter distributions are summarized in Fig. 2b and Fig. 2d. These morphological differences suggest distinct packing/contact geometries and motivate paste-specific kinetic evaluation and profile design.

Under non-isothermal heating (5/10/15 °C·min^{-1}), both pastes show clearly multi-stage mass-loss behavior. Practically, the low-temperature stage is dominated by solvent/low-molecular volatilization and softening, followed by higher-temperature removal of binders/organics (Fig. 3a and Fig. 3d) [20]. The DSC curves exhibit pronounced thermal events around the major mass-loss temperature region, and the peak positions shift toward higher temperatures as the heating rate increases (Fig. 3b and Fig. 3e), consistent with kinetic/thermal lag typical of thermo-analytical measurements. In addition to this overall peak shift, both pastes show a pronounced terminal endothermic feature in the high-temperature region (approximately 270–290 °C), although its sharpness depends on both heating rate and paste formulation. For Paste A, this feature is most pronounced at 10 °C·min^{-1} , whereas for Paste B it becomes most pronounced at 15 °C·min^{-1} . This behavior suggests that the late-stage thermal conversion processes are not manifested as a single isolated event, but rather as a rate- and formulation-dependent overlap of coupled processes, including residual volatile release, organic removal/decomposition, and associated heat-flow responses. Under certain heating-rate conditions, these coupled events appear to be compressed into a narrower temperature interval, leading to a sharper apparent endothermic peak. From a process-design standpoint, these results emphasize that organic removal spans a non-negligible temperature interval [13,14]. Therefore, a controlled heating rate and appropriately placed intermediate dwell(s) are necessary to mitigate risks associated with organic retention or abrupt volatilization (e.g., pore coarsening and interface-defect formation), especially when translating laboratory kinetics into executable furnace programs [30].

To convert thermo-analytical signals into engineering-usable kinetic descriptors, the conversion fraction α was defined from the TGA mass-loss process, and $\alpha(T)$ curves were constructed for both pastes (Fig. 3c and Fig. 3f) [20]. These $\alpha(T)$ curves provide the quantitative basis for subsequent kinetic fitting and for mapping "temperature/time ↔ conversion" during profile design.

Avrami-type fitting was applied to the conversion evolution $\alpha(T)$, yielding kinetic parameters summarized in Table 2 [21]. The fitting quality is acceptable for engineering-scale use ($R^2 \approx 0.80$–0.93), indicating that the simplified Avrami representation captures the dominant conversion behavior sufficiently for profile translation. The fitted Avrami exponent is $n \approx 1.45$–1.70 for Paste A and $n \approx 1.63$–1.77 for Paste B (Table 2), suggesting that the principal conversion behavior for

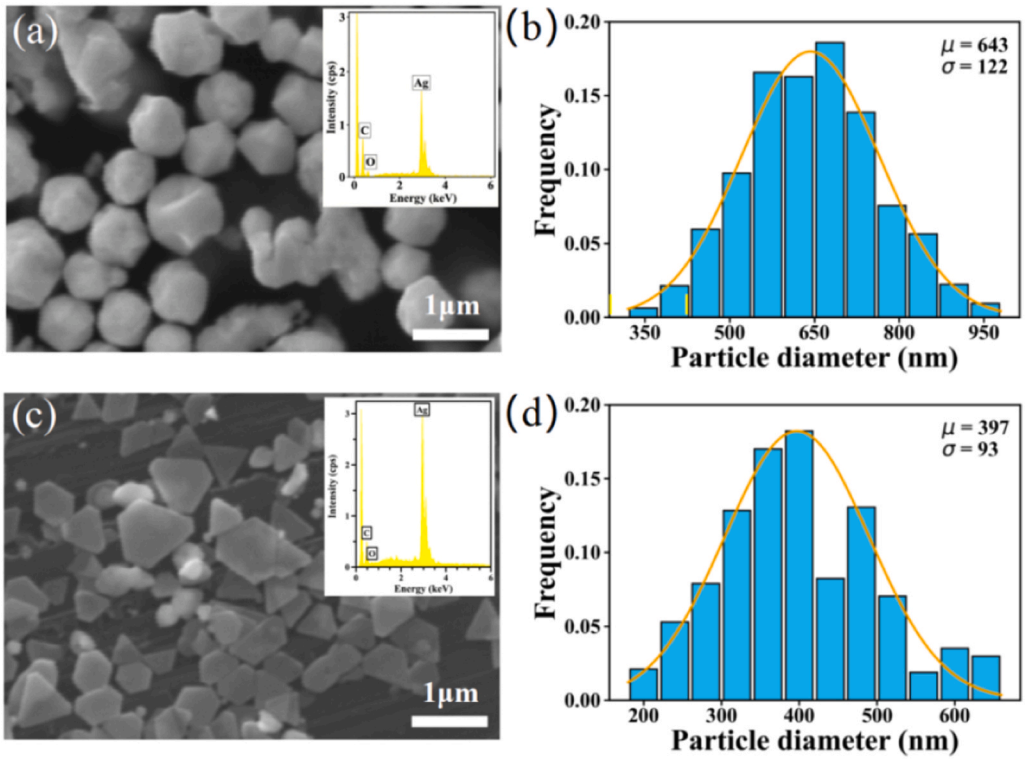


Fig. 2. As-received Ag powder characteristics for Paste A and Paste B. (a,c) Representative SEM micrographs of the as-received Ag powders/pastes for A and B (insets: EDS spectra). (b,d) Corresponding particle diameter distributions with the fitted distribution/summary statistics (mean and standard deviation).

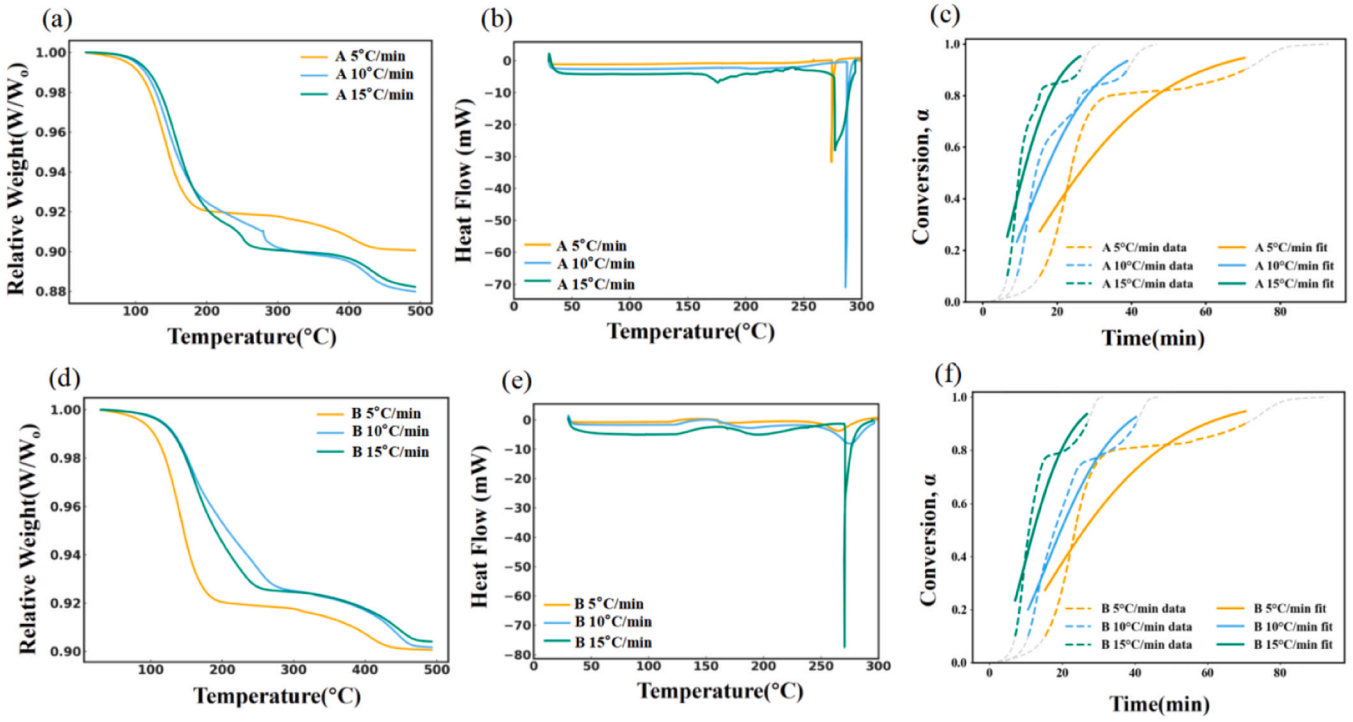


Fig. 3. Thermal analysis and kinetic fitting used to guide profile optimization. (a,b) TGA and DSC responses of Paste A measured at multiple heating rates, showing staged mass-loss behavior and the associated thermal events. (c) Conversion evolution *α(T)* derived from the thermal analysis for Paste A and the corresponding JMAK/Avrami-type kinetic fit. (d,e) TGA and DSC responses of Paste B under the same heating-rate set. (f) *α(T)* for Paste B with the corresponding kinetic fit. Extracted kinetic parameters are summarized in Table 2.

Table 2
Avrami Fitting Parameters of Silver Pastes A and B at Different Heating Rates.

Paste	Heating Rate (°C/min)	k (min^{-n})	n	R^2
A	5	0.006194	1.447	0.802
A	10	0.007626	1.605	0.918
A	15	0.011988	1.696	0.863
B	5	0.005644	1.627	0.811
B	10	0.003421	1.767	0.930
B	15	0.008773	1.747	0.862

both systems can be approximated by a "nucleation–growth-like" formalism at a phenomenological level. Meanwhile, the rate constant k lies at the 10^{-3} –10^{-2} scale (Table 2), indicating a clear time scale for conversion progression, which is essential for mapping "dwell time ↔ target conversion" in a programmable thermal profile.

With the fitted conversion kinetics, the isothermal holding time required to reach a target conversion can be predicted. Fig. 4a provides the predicted holding times for representative conversion targets ($\alpha = 0.97/0.99$) at multiple isothermal temperatures for each paste. Notably, the predicted times decrease systematically with increasing temperature; this trend enables a practical "temperature–time trade-off" map for selecting a feasible dwell window under furnace constraints.

To transform the "conversion–temperature/time" kinetic information (Figs. 2–4) into an executable furnace program, the optimized profiles followed a pragmatic principle: keep the low-temperature solvent/organic-removal segment identical to the supplier (Original) profile, and reconfigure only the mid-/high-temperature densification-related dwell temperature and duration according to the kinetics-based holding-time requirement at the chosen target α^* (Fig. 4) [3,5]. This strategy is intentionally conservative for the volatile-removal stage (to avoid introducing new defect sources), while strengthening the densification window where the conversion kinetics indicates a clear dwell-time requirement.

Based on Fig. 4a, two holding-time values were selected as key design anchors for the optimized profiles: reaching $\alpha = 0.99$ requires 36.74 min at 310 °C for Paste A and 41.17 min at 280 °C for Paste B. These anchors were used to set the main high-temperature dwell in the Optimized schedules (Fig. 4), while the remaining segments were arranged as a segmented program compatible with a programmable box furnace. The resulting Original vs Optimized temperature–time histories for Paste A and Paste B are compared in Fig. 4.

3.2. *Experimental validation of designed profiles*

Shear strength τ was calculated by normalizing the peak shear load by the nominal bonded area (Fig. 5a). Each condition was tested with n = 7, and scatter/box representations were used to capture dispersion. The optimized profiles increased the average shear strength in both paste systems; however, the magnitude of improvement was markedly different. Paste A increased from 21.06 ± 4.99 MPa to 28.37 ± 6.17 MPa, indicating a comparatively modest enhancement, whereas Paste B increased from 9.00 ± 4.01 MPa to 27.54 ± 6.56 MPa, showing a much more pronounced response to profile optimization.

Strength enhancement was accompanied by a systematic fracture-mode shift from interface-dominated failure toward mixed/through-Ag-layer failure [8,27]. Using the Type A/B/C scheme in Fig. 5b (Type C defined as mixed-mode), Paste A changed from Type A-dominant (55 %) to Type C-dominant (69 %), while Paste B changed from Type B-dominant (83 %) to a near-balanced Type C (47 %) and Type B (46 %) distribution after optimization (Fig. 5c). Overall, the increased fraction of Type C indicates a strengthened interface such that failure becomes increasingly governed by cohesion within the Ag layer rather than by adhesive debonding at a single interface. Fracture-mode proportions in Fig. 5c were quantified specimen by specimen for the same seven joints used in the shear test under each condition, and the bars represent mean values with error bars denoting ±1 SD.

To further interpret the different strength responses of the two

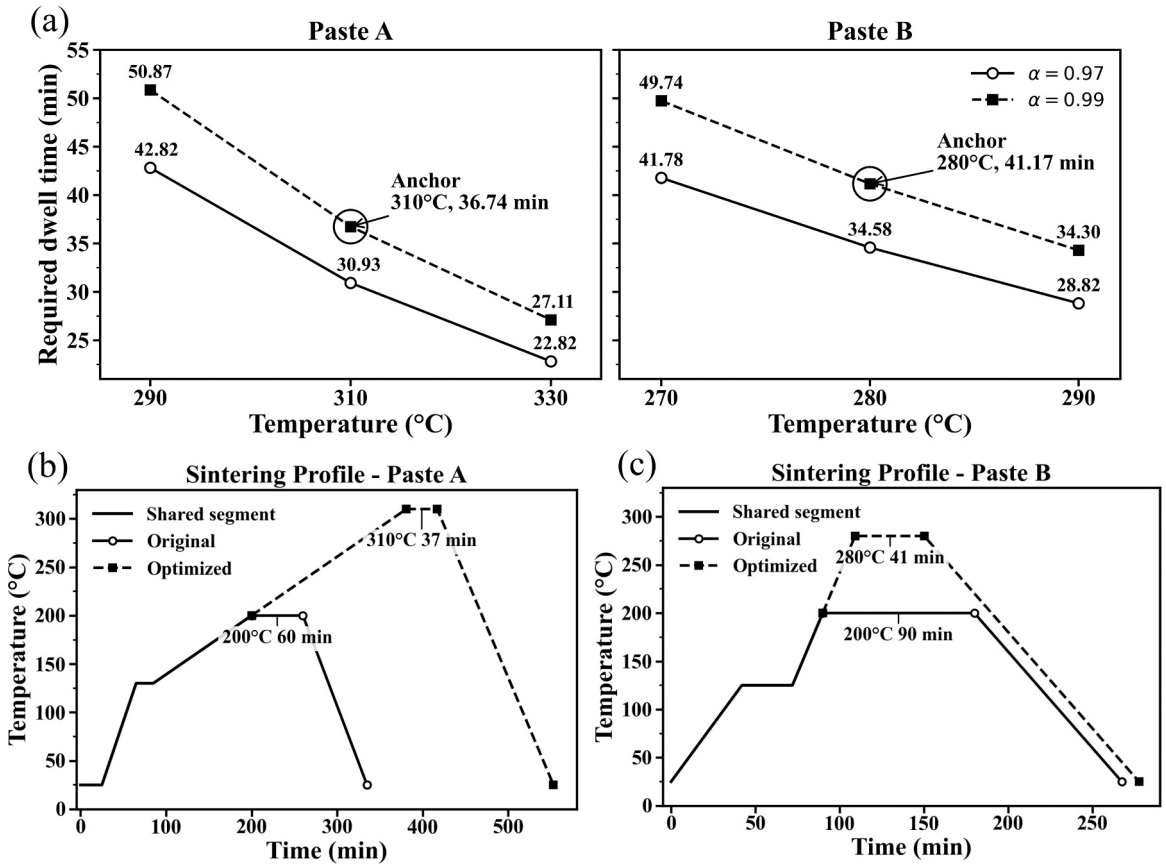


Fig. 4. (a) Kinetics-derived temperature–time trade-off maps for profile selection. Required dwell time as a function of isothermal temperature for target conversion fractions of α = 0.97 and 0.99 for Paste A and Paste B. The selected design anchors used for constructing the optimized furnace profiles are highlighted. (b,c) Original (manufacturer-recommended) and kinetics-guided optimized sintering profiles. Temperature–time histories for (b) Paste A and (c) Paste B, comparing the baseline "Original" profile with the proposed "Optimized" profile. The profiles are shown as segmented schedules, including a shared preprocessing/debinding segment followed by the subsequent sintering segment. The optimized design adjusts the ramp/hold windows to better align with the thermal/kinetic activity intervals identified in Fig. 3.

pastes, bondline-level cross-sectional porosity and post-sintering bondline thickness were additionally quantified from metallographic cross-sectional SEM images (Fig. 5d–f). Compared with Paste A, Paste B shows a more pronounced reduction in cross-sectional porosity and bondline thickness after profile optimization, consistent with its much larger increase in shear strength. By contrast, Paste A exhibits a comparatively smaller structural change, which is consistent with its more modest strength enhancement. These cross-sectional results therefore provide direct quantitative support for the different optimization sensitivities of the two paste systems. It should be noted that the porosity metric in Fig. 5e represents a bondline-level cross-sectional quantity, whereas the Po descriptor in Fig. 8 is a patch-level local descriptor used for heterogeneity analysis.

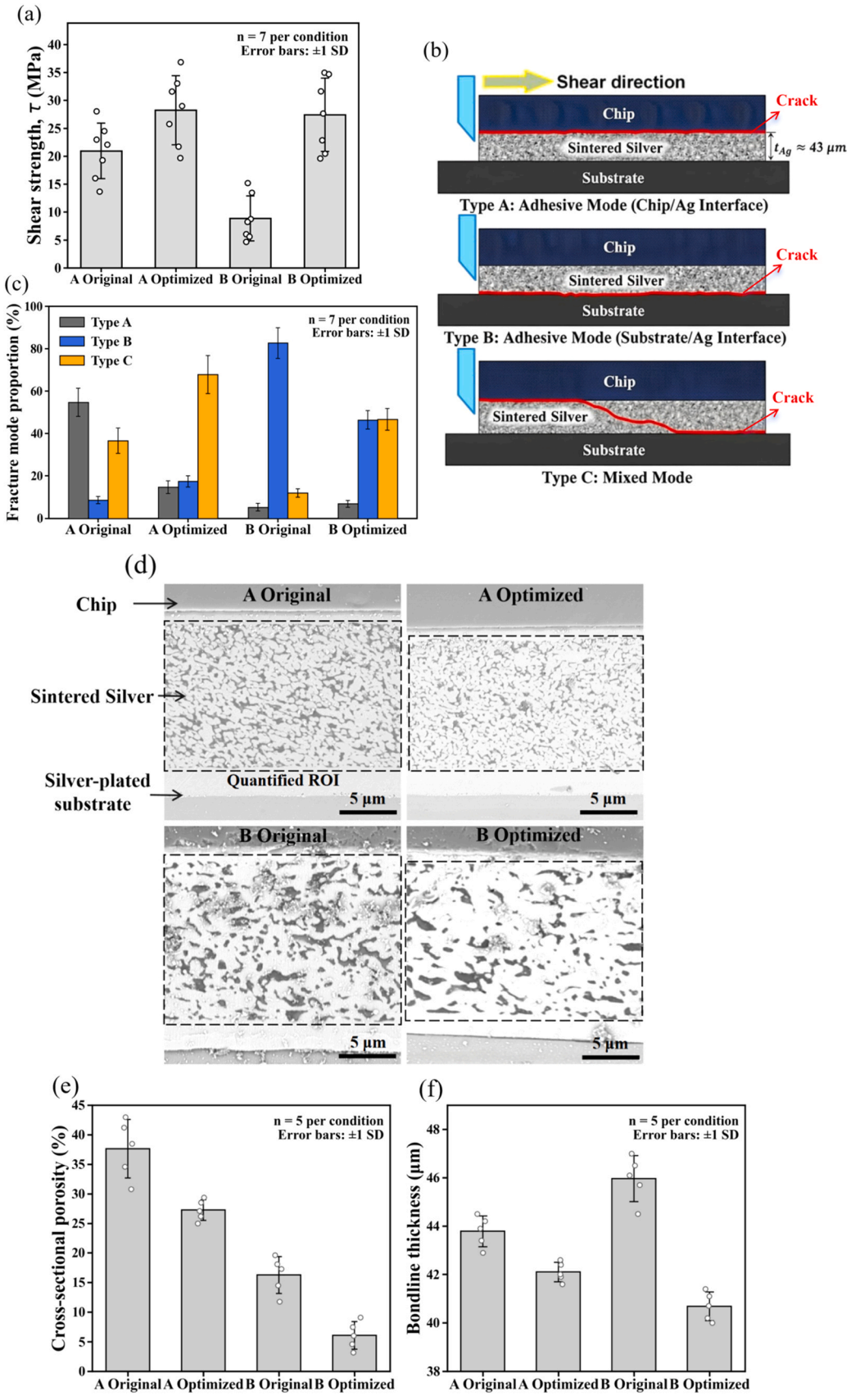
Fig. 6 further establishes a macro–micro morphological evidence chain for this transition using the combined format of macro optical fracture-surface images (main panels) plus two SEM magnifications (right-side panels). The red annotations highlight representative sintering necks/ligaments, providing localized morphological evidence of neck development and connectivity features on the fracture surfaces. These observations are interpreted together with the newly added cross-sectional porosity and bondline-thickness quantification, thereby linking fracture-mode transition to both local morphological characteristics and bondline-level structural evolution.

3.3. Microstructure quantification and heterogeneity

To interpret the strength/mixedness trends validated in Section 3.2, the sintered Ag layer was quantified using a patch-based SEM representation that preserves local heterogeneity. Because pressureless sintered Ag layers often exhibit clustered voids and spatially varying neck-network compactness, patches were adopted as the minimum analysis unit. Each SEM image (acquired at unified magnification/resolution settings) was partitioned into a fixed 3× 3 grid (nine non-overlapping patches). Each patch was independently segmented and quantified, and each condition was then represented as a bag of patches, enabling microstructure to be described as a distribution rather than by a single global mean. This patch-wise representation is consistent with the macro–micro evidence chain in Section 3.2, where failure and mixedness can be governed by localized weak regions rather than by average porosity alone.

A candidate pool of SEM-derived descriptors was first extracted from each patch and then screened to obtain a compact and physically interpretable set for downstream linkage analyses. Fig. 7 summarizes the PCA-based feature screening and the final definition of five core descriptors retained in this work:P_o, P_s, F_a, D_f, and R_a^*. These descriptors were selected as top-ranked and physically complementary variables, balancing redundancy reduction and interpretability for subsequent correlation/regression and MIL analyses.

The physical relevance of the retained descriptors can be interpreted as follows. P_o primarily reflects the local pore content and is therefore directly related to the available solid fraction for neck formation and load transfer. P_s reflects the characteristic size of connected particle domains and is thus relevant to local coalescence/fusion state and the continuity of the solid skeleton. F_a describes particle/domain roundness



(caption on next page)

Fig. 5. Mechanical response, fracture-mode statistics, and bondline-level cross-sectional structural quantification across conditions. (a) Die shear strength τ for A Original, A Optimized, B Original, and B Optimized, shown as mean ± 1 SD with individual measurements overlaid (n = 7 per condition). (b) Representative optical fracture-surface images illustrating the three fracture-mode categories (Type A/B/C) used for quantification. (c) Area-fraction statistics of the fracture-mode categories, quantified specimen by specimen for the same seven joints used in the shear test; bars represent mean values and error bars denote ± 1 SD (n = 7 per condition). (d) Representative metallographic cross-sectional SEM images for the four conditions; dashed boxes indicate the quantified bondline ROI used for cross-sectional porosity analysis. (e) Bondline-level cross-sectional porosity quantified from the full bondline ROI. (f) Post-sintering bondline thickness quantified from metallographic cross-sections. In (e) and (f), bars represent mean values and error bars denote ± 1 SD (n = 5 per condition).

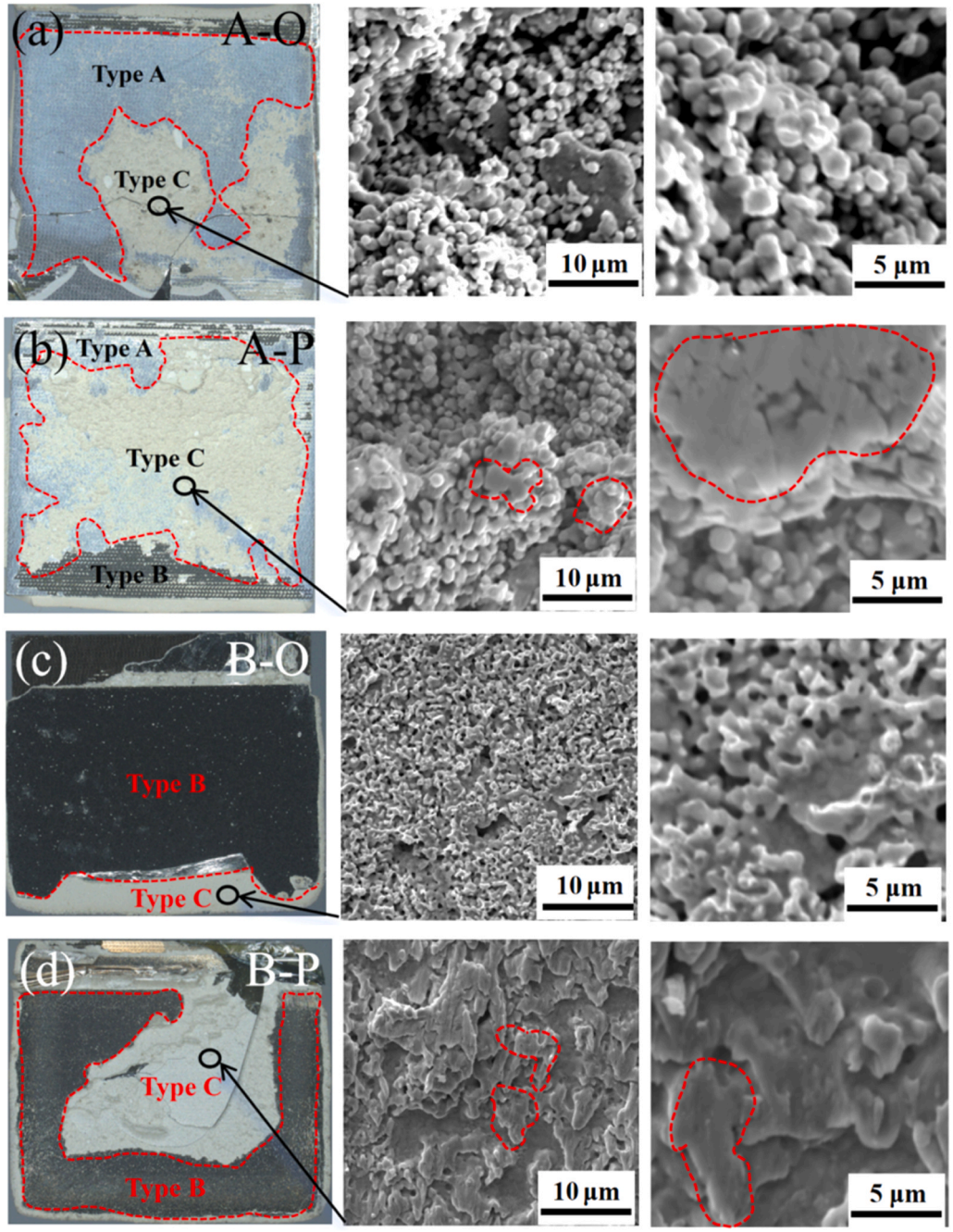


Fig. 6. Representative fracture surfaces and micro-morphologies for the four conditions: (a) A Original, (b) A Optimized, (c) B Original, and (d) B Optimized. For each condition, the left image is an optical macrograph of the overall fracture surface with the fracture-mode regions (Type A/B/C) annotated; the black arrow indicates the SEM sampling location. The two images on the right show the corresponding SEM morphologies at higher magnifications. Red dashed outlines in SEM highlight representative sintering necks/ligaments within the sintered Ag layer.

and fusion uniformity, and can therefore be associated with local morphology regularization during sintering. D_f characterizes the number density of local morphological features per unit area and is relevant to local structural complexity and defect-population intensity. The roughness proxyR_a^* provides complementary information on gray-scale fluctuation and local surface-texture irregularity, and is therefore related to microstructural heterogeneity not fully captured by binary

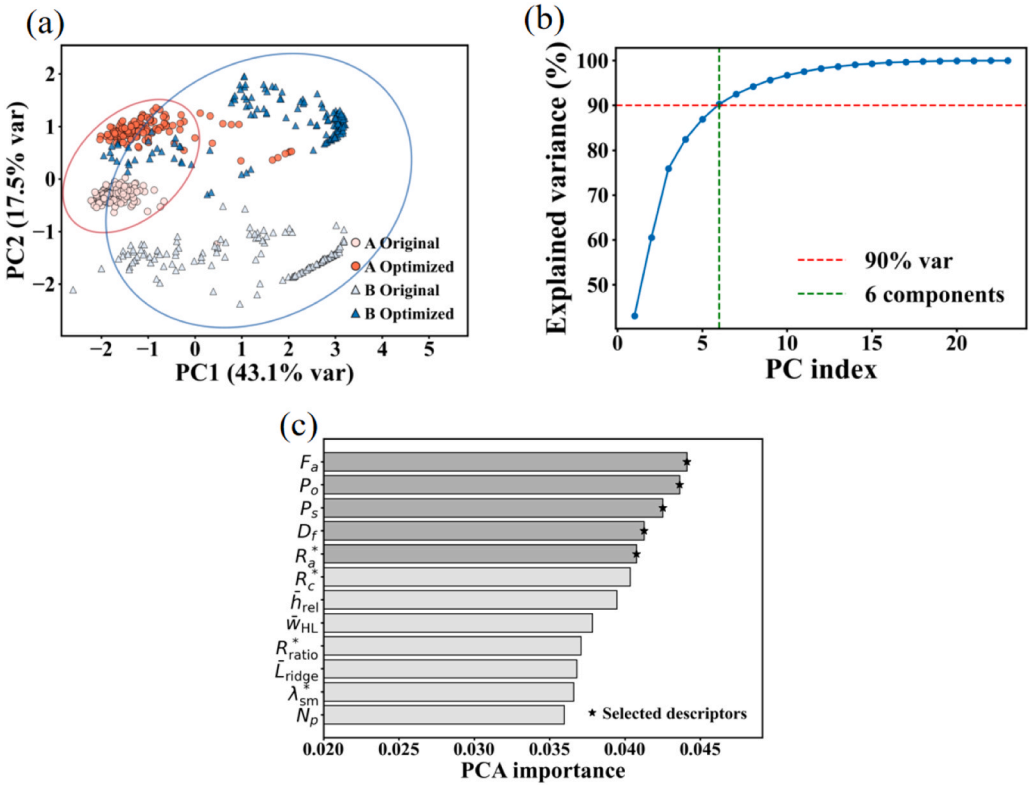


Fig. 7. PCA-based feature screening and definition of SEM-derived descriptors. (a) PCA score plot showing the separation among conditions using the full candidate descriptor set extracted from SEM patches. (b) Cumulative explained variance as a function of the number of principal components, with the selected dimensionality indicated. (c) PCA-based feature contribution/importance used to select five core descriptors (P_o,P_s,F_a,D_f,R_a^*) for subsequent correlation/regression and MIL analyses.

geometric descriptors alone. Taken together, these retained descriptors do not represent one-to-one mechanistic variables, but rather a compact set of physically interpretable proxies for pore connectivity, neck-development conditions, local heterogeneity, and fracture-relevant structural variability. In this sense, higher-order directional and spatial-organization information is captured indirectly through the retained descriptor set rather than through a single explicit variable.

Fig. 8 summarizes the distributions of the five descriptors across the four conditions and further decomposes the statistics into All/H/V subsets. Two consistent observations emerge. First, systematic shifts in medians and interquartile ranges from Original to Optimized profiles are observed within each paste system, providing microstructural evidence that the kinetics-informed dwell modifications in Section 3.1 translate into measurable structural changes, consistent with the strength and fracture-mode validation in Section 3.2. Second, the within-condition spread and the H/V decomposition highlight that the microstructure is not strictly homogeneous and can exhibit direction-dependent differences at the patch scale. This motivates heterogeneity-aware attribution in Section 3.4, because the specimen-level responses (τ and mixedness m) may be disproportionately controlled by a subset of critical patches rather than by global averages.

3.4. Mechanistic interpretation via interpretable analysis

To provide an interpretable first-order linkage between SEM-derived descriptors and macroscopic responses, Pearson correlations were computed between each descriptor and (i) mean shear strength τ and (ii) fracture mixedness m. The results are summarized in Fig. 9. Overall, porosity/connectivity-related descriptors show the most direct associations with τ and m, while texture/feature proxies contribute complementary sensitivity to local morphological variations. These baseline correlations are directionally consistent with the microstructural differences in Section 3.3 and the macroscopic validation trends in Section 3.2.

Because the five descriptors are not strictly independent, ridge regression with standardized inputs was further used to mitigate collinearity and to compare coefficient directions under a multivariate view. The ridge coefficients (Fig. 9) preserve the main ranking trend suggested by Pearson correlations while providing a more stable interpretation under descriptor coupling. Together, Pearson and ridge baselines establish a consistent reference for the subsequent heterogeneity-aware MIL analyses.

To explicitly account for patch-wise heterogeneity, an attention-based MIL model was trained to relate patch-level descriptors to bag-level shear strength τ under the present four-condition dataset [22]. In addition to condition-level agreement, two interpretability outputs were analyzed: (i) gradient-based relative descriptor attribution and (ii) attention concentration, which reflects how strongly a small subset of patches contributes to the bag-level response.

Bag-level prediction agreement is shown by the parity comparison, and Table 3 summarizes the absolute errors across conditions. Fig. 10 reports descriptor importance for predicting τ using all patches and the H/V subsets. The importance ranking is broadly consistent with the linear baselines, indicating that the dominant microstructural controls identified by Pearson/ridge remain influential when heterogeneity is explicitly modeled. Moreover, the attention-concentration results in Fig. 10 demonstrate that a minority of patches can carry a disproportionate fraction of attention mass, supporting the interpretation that localized regions can dominate macroscopic strength.

An analogous MIL analysis was performed for fracture mixedness m, using the same bag/patch formulation. Fig. 11 summarizes the gradient-based relative descriptor importance for predicting mixedness (all patches and H/V subsets), together with attention-based evidence of heterogeneity control. The consistency between the baseline associations (Fig. 9) and MIL attributions (Figs. 10–11) supports a coherent process–structure–property interpretation: the kinetics-guided

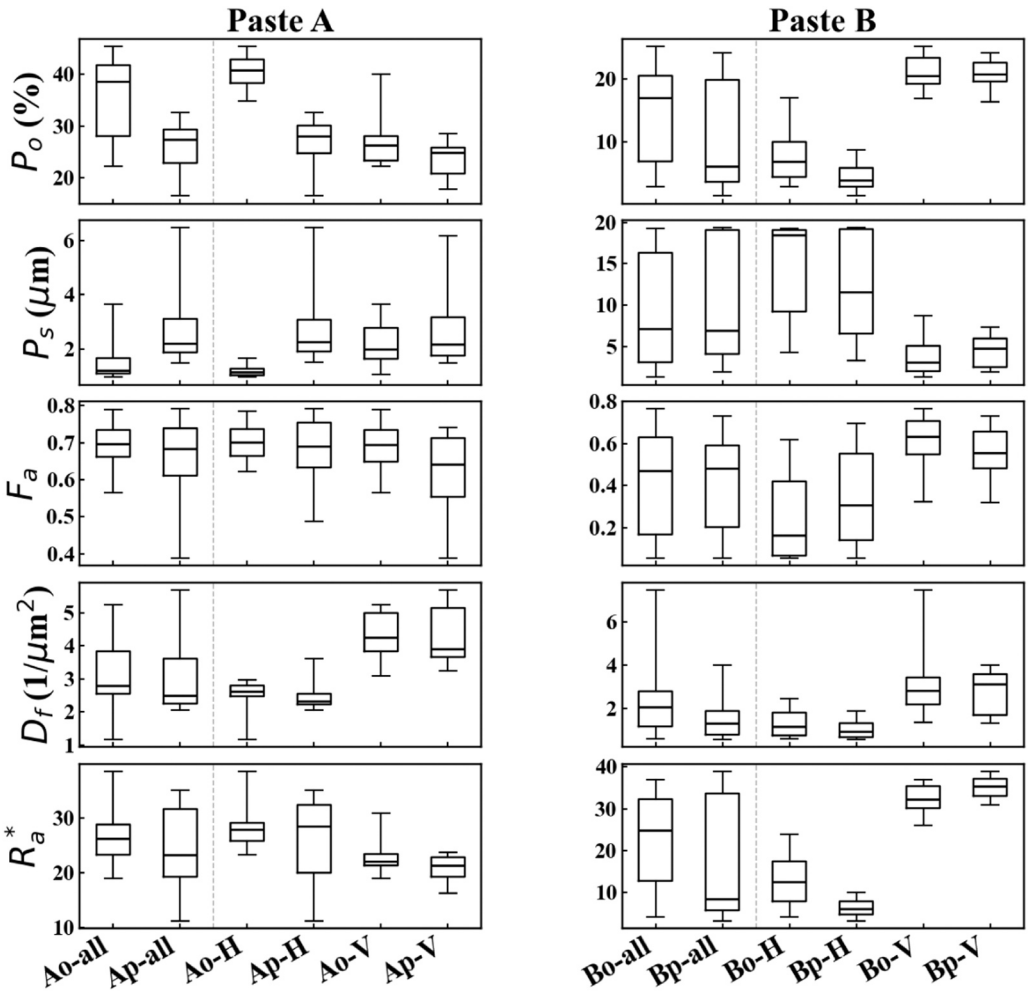


Fig. 8. Distributions of the selected microstructural descriptors across conditions and directions. Boxplots of P_o, P_s, F_a, D_f, and R_a^*comparing Original vs Optimized for Paste A and Paste B. Results are shown for all patches as well as direction-specific subsets (H-direction and V-direction patches), highlighting both process-induced shifts and microstructural directionality.

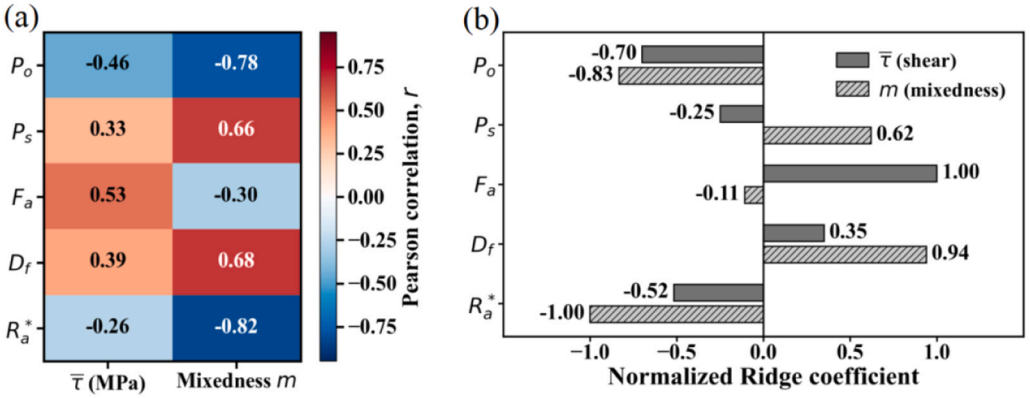


Fig. 9. Baseline "descriptor–property/mode" associations via Pearson correlation and ridge regression. Pearson correlations of the five descriptors with (i) mean shear strength$\bar{\tau}$and (ii) mixedness m (fracture mixed-mode tendency). Ridge-regression coefficients (standardized inputs) are plotted alongside to compare effect directions and relative magnitudes under descriptor collinearity.

adjustment of the densification-related dwell (Section 3.1) induces measurable patch-level microstructural changes (Section 3.3), which in turn improves shear strength and shifts fracture toward more mixed/cohesive participation (Section 3.2). Critically, the attention-concentration behavior indicates that these macroscopic outcomes are often governed by a subset of critical local regions, providing a mechanistic explanation for why global averages alone may be insufficient for interpreting strength and mixedness trends.

It should also be noted that the present workflow was established for the two studied Ag pastes and therefore remains formulation-dependent in its direct applicability. In pressureless sintering systems with stronger solvent-driven or resin-driven out-gassing behavior, the thermal-

Table 3
Bag-level MIL summary for shear strength and fracture mixedness.

Condition	n_{patch}	Shear strength				Mixedness			
		τ_{exp} (MPa)	τ_{pred} (MPa)	$\|\Delta\tau\|$ (MPa)	Top10 mass (%)	m_{exp} (–)	m_{pred} (–)	$\|\Delta m\|$ (–)	Top10 mass (%)
A Original	180	20.95	20.96	0.05	21.8	0.37	0.37	0.03	27.3
A Optimized	180	28.24	28.23	0.04	27.3	0.68	0.68	0.03	31.0
B Original	180	8.86	8.88	0.02	21.0	0.12	0.12	0.05	39.5
B Optimized	180	27.42	27.41	0.04	48.2	0.46	0.47	0.04	40.0

Note: n_{patch} is the number of valid patches retained after identical preprocessing and quality filtering. Top10 mass is defined as $\Sigma_{i=1}^{10}\alpha_{(i)}$ where $\alpha_{(i)}$ are attention weights sorted in descending order within a bag (reported in %). Larger Top10 mass indicates more concentrated attention.

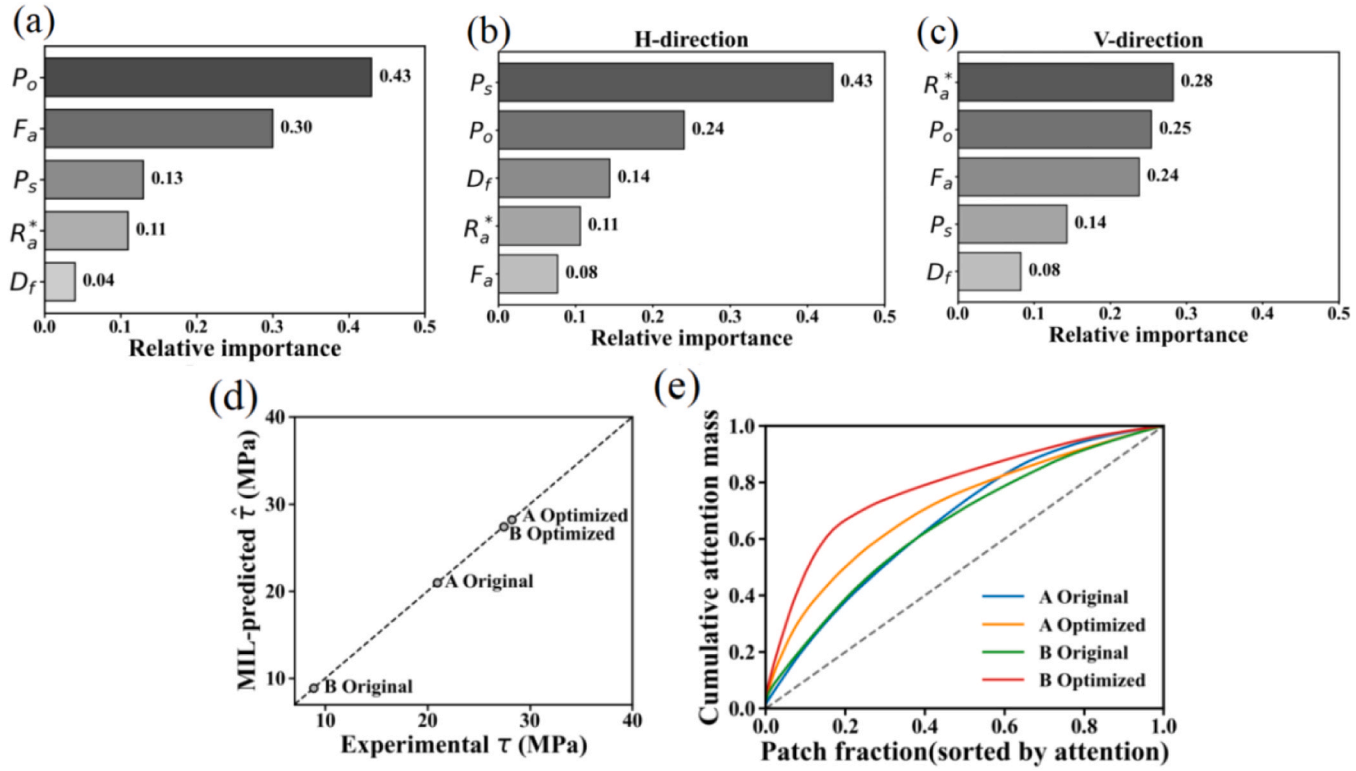


Fig. 10. Attention-based MIL analysis linking patch-level descriptors to shear strength τ. (a–c) Gradient-based MIL relative importance of the five descriptors for predicting τ, computed using (a) all patches, (b) H-direction patches, and (c) V-direction patches. (d) Bag-level parity plot comparing experimental τ and MIL-predicted $\hat{\tau}$ across the four conditions. (e) Cumulative attention-mass curves (patches sorted by attention) characterizing attention concentration within each bag; summary metrics are reported in Table 3.

conversion and volatile-release stages may become more strongly separated or overlapped, which would require additional consideration of staged venting/debinding behavior before direct profile translation. Likewise, practical transfer of the present strategy to paste systems with substantially different organic chemistry, volatile content, or particle-size distribution would require renewed thermo-analytical characterization and formulation-specific re-evaluation. Therefore, while the overall workflow is transferable in principle, its practical implementation should be assessed case by case for paste systems beyond those studied here.

4. Conclusion

In this work, a kinetics-informed sintering-profile design strategy and an explainable, heterogeneity-aware microstructure–property analysis framework were established for two commercial pressureless sintered Ag pastes, and their effectiveness was validated using shear and fracture evidence.

The results are as follows:

1. Multi-rate TGA/DSC combined with Avrami/Arrhenius kinetics enables paste-specific "time-to-target-conversion" prediction and profile translation. Using $\alpha = 0.99$ as the design target, the key dwell anchors were 36.74 min at 310 °C for Paste A and 41.17 min at 280 °C for Paste B.

2. Implementing the optimized profiles in a programmable furnace produces clear mechanical improvement. The shear strength increases from 21.06 ± 4.99–28.37 ± 6.17 MPa for Paste A and from 9.00 ± 4.01–27.54 ± 6.56 MPa for Paste B.

3. Fracture statistics corroborate the strength gains by a consistent shift from interfacial debonding toward mixed/through-Ag-layer failure: Paste A moves from Type A-dominant (55 %) to Type C-dominant (69 %), while Paste B shifts from Type B-dominant (83 %) to a near-balanced Type C/Type B distribution (47 %/46 %).

4. A patch-wise SEM quantification workflow captured microstructural heterogeneity and directionality, and PCA distilled five core descriptors (P_o, P_s, F_a, D_f, and R_a^*). Under the present four-condition dataset, the attention-based MIL analysis provides an interpretable qualitative framework linking patch-level microstructural heterogeneity

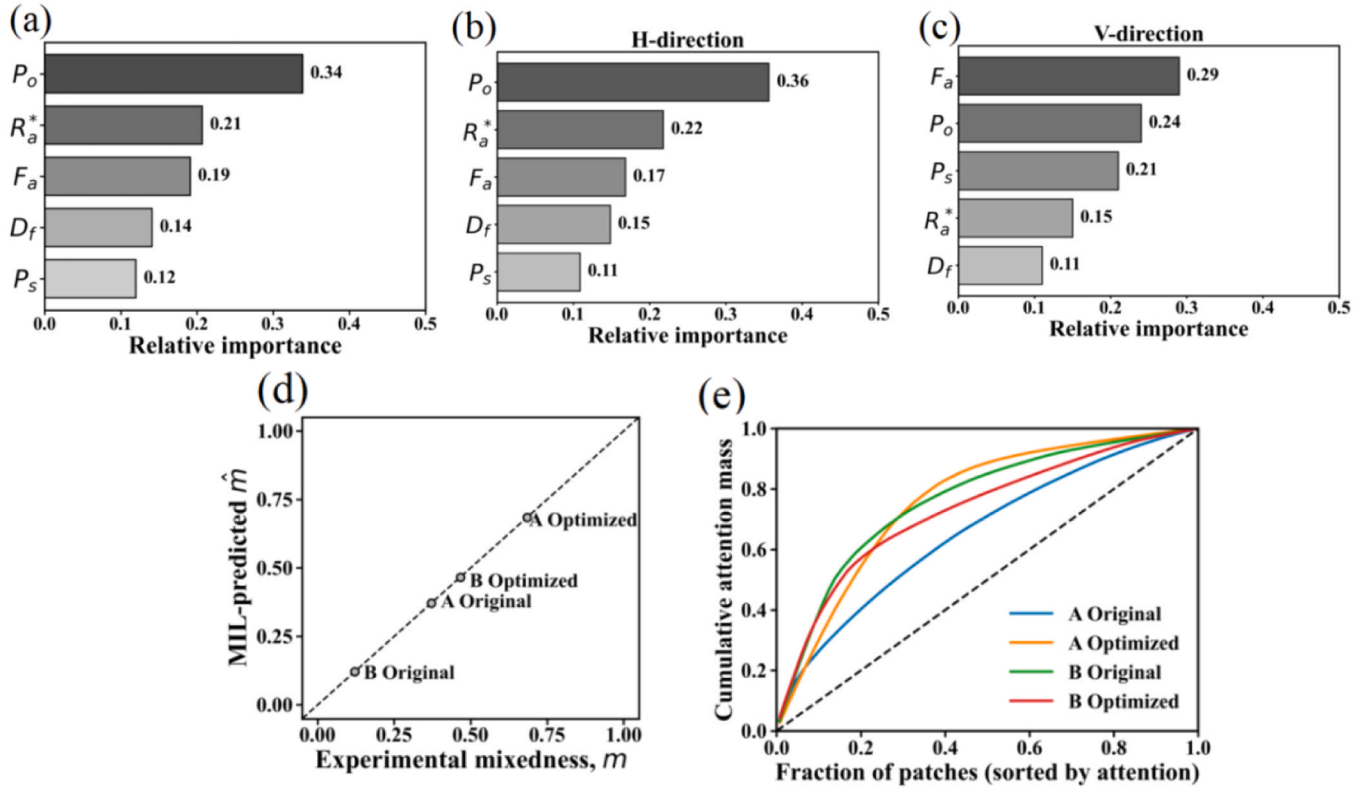


Fig. 11. Attention-based MIL analysis linking patch-level descriptors to fracture mixedness *m*. (a–c) Gradient-based MIL relative importance of the five descriptors for predicting mixedness *m*, computed using (a) all patches, (b) H-direction patches, and (c) V-direction patches. (d) Bag-level parity plot comparing experimental m and MIL-predicted across conditions. (e) Cumulative attention-mass curves (patches sorted by attention) illustrating condition-dependent attention concentration; corresponding bag-level summaries are provided in Table 3.

to condition-level responses (τ and m), while revealing concentrated, direction-dependent attention patterns. These results suggest that a limited subset of patches may exert a disproportionate influence on both responses, thereby connecting macroscopic behavior with localized microstructural zones.

CRediT authorship contribution statement

Jiajie Fan: Writing – review & editing, Validation, Supervision, Resources, Project administration, Funding acquisition, Conceptualization. **Guoqi Zhang:** Supervision, Resources. **Willem van Driel:** Supervision, Resources. **Tiancheng Tian:** Resources, Investigation. **Wei Du:** Writing – review & editing, Investigation. **Zezhan Li:** Writing – original draft, Visualization, Investigation, Formal analysis. **Xueliang Wang:** Writing – review & editing. **Chao Gu:** Writing – review & editing. **Xuyang Yan:** Writing – review & editing.

Declaration of Competing Interest

The authors declare that they have no known competing financial interests or personal relationships that could have appeared to influence the work reported in this paper.

Acknowledgements

The work described in this paper was supported by the National Natural Science Foundation of China (Grant No. 52275559) and China Scholarship Council (Grant No. 202406100064).

Data availability

Data will be made available on request.

References

[1] H.S. Chin, K.Y. Cheong, A.B. Ismail, A review on die attach materials for SiC-based high-temperature power devices, Metall. Mater. Trans. B 41 (2010) 824–832, https://doi.org/10.1007/s11663-010-9365-5.
[2] G. Zeng, S. McDonald, K. Nogita, Development of high-temperature solders: Review, Microelectron. Reliab 52 (2012) 1306–1322, https://doi.org/10.1016/j.microrel.2012.02.018.
[3] S.A. Paknejad, S.H. Mannan, Review of silver nanoparticle based die attach materials for high power/temperature applications, Microelectron. Reliab 70 (2017) 1–11, https://doi.org/10.1016/j.microrel.2017.01.010.
[4] J.G. Bai, J.N. Calata, G.-Q. Lu, Thermomechanical reliability of low-temperature sintered silver die attached SiC power device assembly, IEEE Trans. Device Mater. Reliab 6 (3) (2006) 436–441, https://doi.org/10.1109/TDMR.2006.882196.
[5] S. Wang, M. Li, H. Ji, C. Wang, Rapid pressureless low-temperature sintering of Ag nanoparticles for high-power density electronic packaging, Scr. Mater 69 (2013) 789–792, https://doi.org/10.1016/j.scriptamat.2013.08.031.
[6] C.X. Yang, X. Li, G.-Q. Lu, Y.-H. Mei, Enhanced pressureless bonding by tin doped silver paste at low sintering temperature, Mater. Sci. Eng. A 660 (2016) 71–76, https://doi.org/10.1016/j.msea.2016.02.082.
[7] Y. Xie, Y. Wang, Y. Mei, H. Xie, K. Zhang, S. Feng, K.S. Siow, X. Li, G.-Q. Lu, Rapid sintering of nano-Ag paste at low current to bond large area (>100 mm^2) power chips for electronic packaging, J. Mater. Process. Technol 255 (2018) 644–649, https://doi.org/10.1016/j.jmatprotec.2018.01.017.
[8] J. Carr, X. Milhet, P. Gadaud, S.A.E. Boyer, G.E. Thompson, P. Lee, Quantitative characterization of porosity and determination of elastic modulus for sintered micro-silver joints, J. Mater. Process. Technol 225 (2015) 19–23, https://doi.org/10.1016/j.jmatprotec.2015.03.037.
[9] C. Chen, K. Suganuma, Microstructure and mechanical properties of sintered Ag particles with flake and spherical shape from nano to micro size, Mater. Des. 162 (2019) 311–321, https://doi.org/10.1016/j.matdes.2018.11.062.
[10] C. Chen, S. Nagao, K. Suganuma, et al., Macroscale and microscale fracture toughness of microporous sintered Ag for applications in power electronic devices, Acta Mater 129 (2017) 41–51, https://doi.org/10.1016/j.actamat.2017.02.065.
[11] T. Wang, G. Chen, Y. Wang, X. Chen, G.-Q. Lu, Uniaxial ratcheting and fatigue behaviors of low-temperature sintered nano-scale silver paste at room and high temperatures, Mater. Sci. Eng. A 527 (2010) 6714–6722, https://doi.org/10.1016/j.msea.2010.07.012.
[12] G. Chen, L. Yu, Y. Mei, X. Li, X. Chen, G.-Q. Lu, Uniaxial ratcheting behavior of sintered nanosilver joint for electronic packaging, Mater. Sci. Eng. A 591 (2014) 121–129, https://doi.org/10.1016/j.msea.2013.10.091.

[13] G. Chen, X.-H. Sun, P. Nie, Y.-H. Mei, G.-Q. Lu, X. Chen, High-temperature creep behavior of low-temperature-sintered nano-silver paste films, J. Electron. Mater 41 (2012) 782–790, https://doi.org/10.1007/s11664-012-1903-2.
[14] X. Li, et al., Creep properties of low-temperature sintered nano-silver lap shear joints, Mater. Sci. Eng. A 579 (2013) 108–113, https://doi.org/10.1016/j.msea.2013.05.001.
[15] Y. Tan, X. Li, Y. Mei, G. Chen, X. Chen, Temperature-dependent dwell-fatigue behavior of nanosilver sintered lap shear joint, J. Electron. Packag 138 (2) (2016) 021001, https://doi.org/10.1115/1.4032880.
[16] P. Gadaud, V. Caccuri, D. Bertheau, J. Carr, X. Milhet, Ageing sintered silver: relationship between tensile behavior, mechanical properties and nanoporous structure evolution, Mater. Sci. Eng. A 669 (2016) 379–386, https://doi.org/10.1016/j.msea.2016.05.108.
[17] G. Chen, X. Zhao, Constitutive modelling on the whole-life uniaxial ratcheting behavior of sintered silver joints, Microelectron. Reliab 80 (2018) 47–54, https://doi.org/10.1016/j.microrel.2017.11.010.
[18] Z. Zhang, C. Chen, A. Suetake, M.-C. Hsieh, K. Suganuma, Reliability of Ag sinter-joining die attach under harsh thermal cycling and power cycling tests, J. Electron. Mater 50 (2021) 6597–6606, https://doi.org/10.1007/s11664-021-09221-y.
[19] Z. Cui, Q. Jia, H. Zhang, et al., Review on shear strength and reliability of nanoparticle sintered joints for power electronics packaging, J. Electron. Mater 53 (2024) 2703–2726, https://doi.org/10.1007/s11664-024-10970-9.
[20] S. Vyazovkin, A.K. Burnham, J.M. Criado, L.A. PÉrez-Maqueda, C. Popescu, N. Sbirrazzuoli, ICTAC kinetics committee recommendations for performing kinetic computations on thermal analysis data, Thermochim. Acta 520 (2011) 1–19, https://doi.org/10.1016/j.tca.2011.03.034.
[21] M. Avrami, Kinetics of phase change. I. General theory, J. Chem. Phys 7 (1939) 1103–1112, https://doi.org/10.1063/1.1750380.
[22] M. Ilse, J.M. Tomczak, M. Welling, Attention-based deep multiple instance learning, in: Proc. 35th Int. Conf. Mach. Learn. (ICML 2018), 80, PMLR,, 2018, pp. 2132–2141.
[23] S.M. Lundberg, S.-I. Lee, A unified approach to interpreting model predictions, in: Proceedings of the 31st International Conference on Neural Information Processing Systems, Curran Associates Inc., Red Hook, NY, USA, 2017, pp. 4768–4777.
[24] M. Sundararajan, A. Taly, Q. Yan, Axiomatic attribution for deep networks (Integrated Gradients), in: Proc. 34th Int. Conf. Mach. Learn. (ICML 2017), 70, PMLR,, 2017, pp. 3319–3328.
[25] M.T. Ribeiro, S. Singh, C. Guestrin, "Why Should I Trust You?": Explaining the Predictions of Any Classifier, in: Proceedings of the 22nd ACM SIGKDD International Conference on Knowledge Discovery and Data Mining, 2016, pp. 1135–1144, https://doi.org/10.1145/2939672.2939778.
[26] J. Li, C.M. Johnson, C. Buttay, et al., Bonding strength of multiple SiC die attachment prepared by sintering of Ag nanoparticles, J. Mater. Process. Technol 215 (2015) 299–308, https://doi.org/10.1016/j.jmatprotec.2014.08.002.
[27] S. Zhao, Y. Dai, F. Qin, Y. Li, L. Liu, Z. Zan, T. An, P. Chen, Y. Gong, Y. Wang, On mode II fracture toughness of sintered silver based on end-notch flexure (ENF) test considering various sintering parameters, Mater. Sci. Eng. A 823 (2021) 141729, https://doi.org/10.1016/j.msea.2021.141729.
[28] A.E. Hoerl, R.W. Kennard, Ridge regression: biased estimation for nonorthogonal problems, Technometrics 12 (1) (1970) 55–67, https://doi.org/10.1080/00401706.1970.10488634.
[29] S. Zabihzadeh, et al., Deformation behavior of sintered nanocrystalline silver layers, Acta Mater 97 (2015) 116–123, https://doi.org/10.1016/j.actamat.2015.06.040.
[30] P. Zhao, J. Huang, J. Nan, D. Liu, F. Meng, Laser sintering process optimization of microstrip antenna fabricated by inkjet printing with silver-based MOD ink, J. Mater. Process. Technol 275 (2020) 116347, https://doi.org/10.1016/j.jmatprotec.2019.116347.